Nanoscale

ROYAL SOCIETY OF CHEMISTRY

PAPER

View Article Online
View Journal | View Issue

Cite this: *Nanoscale*, 2025, **17**, 18935

Halloysite nanotubes as a vector for hydrophobic perfluorinated porphyrin-based photosensitizers for singlet oxygen generation†

Hady Hamza,[a,b] Veronica Schifano,[a] Giorgia Colciago,[c] Marco Aldo Ortenzi,[a,d,e] Anna Maria Ferretti,[f] Gabriele Di Carlo,[a,e] Maria Vittoria Dozzi,[a] Riccardo Vago,[c,g] Francesca Tessore[a,e] and Daniela Maggioni*[a,e]

The development of effective drug delivery systems represents a significant advancement in cancer treatment. Anisotropic, natural, and cost-effective nano-vectors, such as halloysite nanotubes (HNT), can be utilized for this purpose. In this study, we loaded the HNT with the apolar photosensitizers (PS) 5,10,15,20-tetrakis(perfluorophenyl)porphyrin (H_2TPPF_{20}) and its Zn(II) complex ($ZnTPPF_{20}$) to produce singlet oxygen for photodynamic therapy (PDT). The loading was achieved through repeated vacuum/N_2 cycles using both pristine HNT and HNT modified with tetradecylphosphonic acid (HNT-TDP) to promote the uptake of the lipophilic PS in the inner lumen. To slow down the release of PS from HNT, the nanotubes were treated with dextrin. The ability of the free base and Zn perfluorinated porphyrins to produce singlet oxygen ($^1O_2$) was confirmed by irradiating the samples with a low-power visible LED emitter (23 mW cm^{-2}), showing a $^1O_2$ quantum yield of 22% and 34%, respectively, in ethanol. The characterization of the nanocomposite is not trivial, so we employed a wide range of analytical techniques to investigate the material thoroughly, particularly the location of PS within the HNT. All nano-hybrids were analyzed by attenuated total reflectance infrared (ATR-FTIR), diffuse reflectance (DRS) and solid-state emission spectroscopy. Thermogravimetric analysis (TGA) was used to determine the loading capacity of HNT. To better understand the interactions between the PS and the nanoclay, we compared all the loaded HNT samples with mechanically mixed HNT and solid H_2TPPF_{20} or $ZnTPPF_{20}$ samples, where the interaction with the HNT inner lumen is assumed to be absent. We measured the release kinetics using UV-vis spectroscopy, observing a delayed release of the PS. Finally, we studied the cellular uptake of pristine HNT and a loaded sample (HNT-TDP-H_2TPPF_{20}-dextrin) by confocal microscopy using three distinct tumor cell lines. The cytotoxicity on PC3, 5637 and UMUC3 cells was then assessed as reduction of cell viability both on cells left in the dark and those irradiated with a visible light emitting LED (1.3 mW cm^{-2}), ascertaining the ability to induce cell death especially after light administration.

Received 13th March 2025,
Accepted 16th July 2025

DOI: 10.1039/d5nr01078k

rsc.li/nanoscale

1. Introduction

Extensive research has been conducted in recent decades on the development of nanocarriers for drug delivery for cancer treatment.[1] This focus stems from the necessity of achieving effective targeted delivery to diseased tissues while minimizing nonspecific biodistribution and its associated unwanted side effects. Nanocarriers help avoid rapid excretion, primarily through renal clearance, relying on their capacity to passively target solid tumours characterized by a loose vasculature with enhanced permeability with respect to healthy tissues. Moreover, nanocarriers can act as a protective shield against early drug metabolism or degradation, possibly succeeding in delivering drugs only at the tumour site. Importantly, nanocarriers are frequently utilized to address the poor solubility of

[a]*Dipartimento di Chimica, Università degli Studi di Milano, Via Golgi 19, 20123 Milano, Italy. E-mail: daniela.maggioni@unimi.it*
[b]*Chemistry Department, Faculty of Science, Alexandria University, P.O. Box 21568, Alexandria, Egypt*
[c]*Urological Research Institute, Division of Experimental Oncology, IRCCS San Raffaele Hospital, Via Olgettina, 60, 20132 Milano, Italy*
[d]*CRC LaMPo (Laboratorio Materiali e Polimeri), Department of Chemistry, Università degli Studi di Milano, Via Golgi 19, 20123 Milano, Italy*
[e]*Consorzio Interuniversitario Nazionale per la Scienza e Tecnologia dei Materiali (INSTM), via G. Giusti 9, 50121 Firenze, Italy*
[f]*Istituto di Scienze e Tecnologie Chimiche "Giulio Natta", CNR, G. Fantoli 16/15, 20138 Milano, Italy*
[g]*Università Vita-Salute San Raffaele, Via Olgettina, 60, 20132 Milano, Italy*
† Electronic supplementary information (ESI) available. See DOI: https://doi.org/10.1039/d5nr01078k

hydrophobic drugs and facilitate their controlled release, often triggered by external stimuli.

Halloysite nanotubes (HNT), which are naturally occurring kaolin minerals presenting a tubular morphology in the micro-range but with a diameter in the nano-range (inner diameter: 15–50 nm, outer diameter: 50–100 nm, Fig. 1), have been exploited for a plethora of biomedical applications in the last few decades,[2] including drug delivery.

Thousands of tons of HNT are available from natural deposits worldwide,[3,4] at a cheap price and thus they have been the object of a huge industrial development. The layer of halloysite consists of one monolayer of SiO_4 tetrahedra combined with one sheet of AlO_6 octahedra, which brings the ideal unit formula for halloysite-7A and halloysite-10A of $Al_2Si_2O_5(OH)_4{\cdot}nH_2O$, where n = 0 and 2, respectively.[5] Interestingly, the roll-up of the kaolin bilayer sheet to form HNT leads to a different composition of the inner lumen (alumina, with exposed Al–OH groups) and outer surface (silica, mostly exposing Si–O–Si and at a certain extent also Si–OH groups) of the nanotube,[6] which causes the inner part to be positively charged[7] and the outer part to show an opposite negative charge. This feature can be exploited for selective loading or reactivity towards a specific reagent,[8–10] and has been reported for drug delivery purposes in many reports,[9,11–20] by either encapsulating drugs in the inner lumen or by adsorbing it on the outer silica surface.[21–24] Nonetheless, some fundamental papers reported on the peculiar ability of elongated nanoparticles to more effectively accumulate at solid tumor sites, highlighting that nanoparticle shape, in addition to surface composition and size, is a key factor influencing biocirculation, biodistribution, cellular uptake and overall drug efficacy.[25] For example, in a recent article,[26] enhanced transport of inorganic nanorods through pores, combined with reduced viscous resistance near the vessel walls, allowed for faster tumor penetration compared to nanospheres, influencing their biodistribution. The comparison of HNT with mesoporous silica nanoparticles (MSN), a class of synthetic porous NPs often proposed for drug delivery and that present the same chemical composition of the HNT outer surface, highlights how HNT have a much larger lumen diameter than MSN pores, allowing them to accommodate a significantly higher amount of guest molecules and possibly also of bigger size. Nevertheless, the fate of inorganic nanomaterials once administered is an issue that must be addressed, and *in vivo* long term pharmacokinetics and pharmacodynamics studies should ascertain their applicability at the clinical level. In this regard, several studies have appeared in the literature aiming at the clinical translation of inorganic nanoparticles, based on silica, iron oxide and gold, as well as on their nanocomposites.[27,28] Currently, several preclinical studies have demonstrated the use of HNT in cancer therapy, administered either intratumorally or intravenously, resulting in tumor growth inhibition across various mouse models without significant toxic effects.[29]

The objective of this study is to develop appropriately modified HNT for the possible *in situ* delivery of a suitable apolar photosensitizer for photodynamic therapy (PDT). PDT has garnered significant attention in recent decades[30] due to its minimally invasive nature and effectiveness in treating various diseases, including several types of cancer and bacterial infections. PDT relies on three key components: visible or near-infrared (NIR) radiation, a photosensitizer (PS), and molecular oxygen within the tissues,[31] and involves the formation of toxic species either by an electron transfer (Type I PDT) to form radical species or an energy transfer process (Type II PDT), resulting in the generation of the highly cytotoxic singlet oxygen ($^1O_2$*). The highly reactive species produced during Type I and Type II PDT can damage nucleic acids, lipids, and proteins. It is important to emphasize that numerous studies suggest that Type II reactions are particularly potent,[32] primarily due to the predominance of singlet oxygen production.

The majority of PS currently employed in PDT belongs to the category of porphyrins and their analogues.[31,33] Porphyrins, a class of tetrapyrrolic macrocycles, possess an extended 18-electron π-conjugated system, resulting in strong absorptions in the visible light spectrum. Their structure can be rationally designed with specific functionalities, allowing for fine-tuning of their chemical–physical properties and electronic features.[34] These characteristics make porphyrins ideal chromophores in various applications, including non-linear optics (NLO),[35] photovoltaics (PV),[36,37] artificial photosynthesis,[38,39] and in biomedicine.[40] Their strong absorption in the visible light spectrum enables deep tissue penetration, and long-wavelength fluorescence emissions, making them ideal for diagnostic purposes in tumor imaging.[41] Moreover, their visible light absorptions, which enable deep tissue penetration, and their ability to generate reactive oxygen species (ROS) upon light irradiation, make porphyrins particularly suitable as PS in PDT. Also, they exhibit low dark cytotoxicity, being relatively harmless in the absence of light, generate reactive oxygen species (ROS) upon light irradiation and are preferentially taken up by cancer cells.[42]

In this work, we chose the perfluorinated and apolar porphyrin 5,10,15,20-tetrakis(pentafluorophenyl)porphyrin

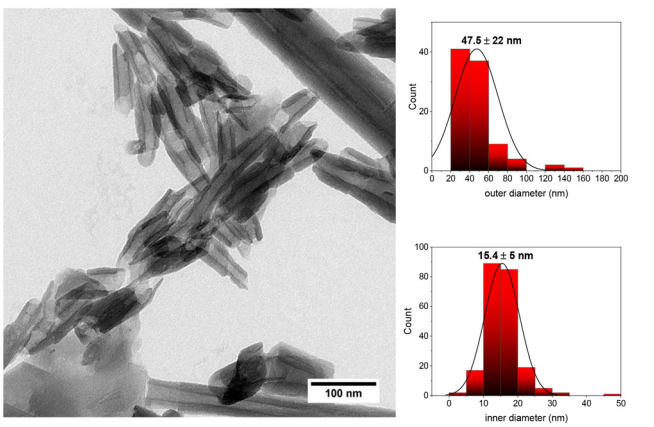

Fig. 1 TEM image of pristine HNT with size distributions of inner and outer lumens.

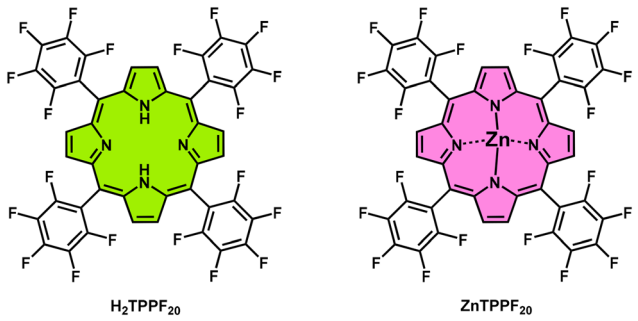

Fig. 2 Chemical structure of porphyrins used in our work: the free base form H_2TPPF_{20} and its Zn(II) complex $ZnTPPF_{20}$.

(H_2TPPF_{20}) and its Zn(II) complex ($ZnTPPF_{20}$) (Fig. 2) as the PS to be loaded onto HNT. The literature reports the use of partially or totally fluorinated porphyrins in combination with clays (kaolinite,[43] HNT,[44,45] metakaolinite and meta-HNT[46]) for catalysis purposes. Moreover, the photocatalytic properties of H_2TPPF_{20} and $FeTPPF_{20}$ were also investigated in combination with a Mg–Al hydrotalcite anionic clay for the photocatalytic aerobic epoxidation of alkenes under visible light irradiation.[47] At the same time, to the best of our knowledge, only one HNT–porphyrin adduct proposed for PDT applications has appeared recently in the literature, but employing the non-fluorinated tetracarboxyphenylporphyrin grafted at the external surface of HNT previously functionalized with Mn (III) ions.[48]

Hereafter, H_2TPPF_{20} and $ZnTPPF_{20}$ will serve as models for apolar drugs that face solubility challenges in aqueous environments. Indeed, their ability to act as photosensitizer is well known even though in apolar solvents,[49,50] or in water, provided that a further functionalization endows the H_2TPPF_{20} with polar groups.[51] Hence, first of all, we ascertained the ability of H_2TPPF_{20} and $ZnTPPF_{20}$ to act as photosensitizers for the production of singlet oxygen in a more polar solvent such as ethanol, even in the absence of further functionalization for enhancing their solubility.

We then used the well-known method reported as "vacuum-assisted loading"[52] that employs repeated vacuum/N_2 cycles to load H_2TPPF_{20} and $ZnTPPF_{20}$ into both pristine HNT and HNT modified with tetradecylphosphonic acid (HNT-TDP),[53] with the aim of obtaining a more apolar inner environment. Indeed, the binding of the phosphonic acid head groups to the inner surface results in the exposure of the hydrophobic tails, thereby imparting a hydrophobic character to the inner lumen,[54] which is expected to be more effective in promoting preferential inner lumen loading of the hydrophobic perfluorinated porphyrin-based PS. The inner location of the perfluorinated porphyrins could greatly benefit the use of the nanocomposite in PDT, as oxygen – known for its high affinity for fluorine atoms – could be effectively adsorbed onto the inner lumen and act as a reservoir of O_2 for hypoxic solid tumors.[55] Proving the (outer or inner) localization of the guest molecules in HNT is not trivial (especially if the guest molecule is neutral as in our case); hence, we employed different analytical techniques, such as ATR-FTIR, DRS, solid state emission spectroscopy as well as TEM microscopy to get hints about the main localization of the porphyrins. We also compared the TGA results obtained for the PS alone with those for the vacuum-loaded pristine HNT and TDP-modified HNT, as well as with mechanically mixed HNT with H_2TPPF_{20} or $ZnTPPF_{20}$, which we prepared for comparison purposes, since in these ground samples, the interaction of the porphyrin with HNT, if any, was expected to be only with the silica-base external part of the nanoclay. The HNT and HNT-TDP loaded samples were covered with a polymer agent (dextrin), and we measured the porphyrin release, comparing it with that of the untreated HNT samples and the ground ones. Finally, the different organic–inorganic composites were tested on three different tumor cell lines to assess their ability to be internalized and reduce cell viability after an appropriate irradiation time with visible light.

2. Results and discussion

2.1 Photoreaction of H_2TPPF_{20} and $ZnTPPF_{20}$ with 1,5-dihydroxynaphthalene as an indirect reporter of $^1O_2$ formation

The ability of H_2TPPF_{20} and $ZnTPPF_{20}$ to act as photosensitizers (PS) for $^1O_2$ generation is well known, but due to the good solubility of these molecules in apolar solvents, literature data do not report on their behaviour in polar ones.[49,50] Indeed, the aggregation could cause a partial or total quench of their emitting properties and hence also the quench of singlet oxygen generation. Here, we showed that even in a polar solvent such as ethanol, these perfluorinated molecules are even able to produce the cytotoxic $^1O_2$. To this aim, we used 1,5-dihydroxynaphtalene (DHN) as an indirect reporter of singlet oxygen. DHN reacts promptly, quantitatively, and selectively with $^1O_2$ forming the oxidized species Juglone (5-hydroxy-1,4-naphthalenedione)[56–58] according to Scheme S1.†

We carried out the experiments by adding one of the two PS to an ethanol DHN solution. After being saturated with O_2, the mixture was irradiated with a visible-light emitting LED (23 mW cm^{-2}), monitoring the evolution of the species by UV-vis spectroscopy. In particular, we observed the decrease of the DHN band at 317 nm and the concomitant increase of the large Juglone band centred at 423 nm, which in our case was partly overlapped with the very strong Soret band of the PS (Fig. S1†). The conversion from DHN to Juglone occurs without the formation of long-lived intermediates or by-products as indicated by the two isosbestic points at 275 and 335 nm observed in the spectra recorded during the irradiation in ethanol solution. Fig. S1d† shows the first-order semilogarithmic plots for the reaction of eqn (1), sensitized by H_2TPPF_{20}, $ZnTPPF_{20}$ or methylene blue (MB), employed as standard for the determination of the singlet oxygen formation quantum yield.

$$\mathrm{DHN} + {}^1\mathrm{O_2} \rightarrow \mathrm{Juglone} + \frac{1}{2}{}^3\mathrm{O_2} \quad (1)$$

The disappearance of DHN (Fig. S1d†) was used for evaluating the singlet oxygen (Φ_Δ) generation quantum yields (see the

Table 1 Estimated quantum yields of singlet oxygen production Φ_Δ, kinetic constants (k_{obs}) and starting rates (ν_i) of MB, H_2TPPF_{20} and $ZnTPPF_{20}$ in ethanol

Compound name	k_{obs} (min^{-1})	ν_i	Φ_Δ
MB	0.0253	3.80×10^{-6}	0.50
H_2TPPF_{20}	0.0017	2.96×10^{-7}	0.22
$ZnTPPF_{20}$	0.0021	3.65×10^{-7}	0.34

experimental part for details) attained with the investigated PS, and the results are reported in Table 1. Even though these apolar porphyrins are partly aggregated in ethanol, they were still able to interact with molecular oxygen and, through an energy transfer, produce the cytotoxic singlet oxygen under the stimulus of a visible low-intensity light.

2.2 Drug loading

To assess the capability of HNT in loading, an apolar drug within its inner lumen, two sets of loaded HNT samples were prepared. In one instance, pristine HNT was used, while in the second one, modified HNT functionalized within the inner lumen was employed. This modification involved the grafting of the apolar tetradecylphosphonic acid molecules selectively onto the inner alumina surface (HNT-TDP),[53,54] by exploiting the very well-known selective reactivity of the alumina inner layer towards phosphonic moieties.[59] The two HNT samples were treated with both H_2TPPF_{20} and $ZnTPPF_{20}$ by dissolving the porphyrins in ethanol in the presence of the suspended pristine HNT or HNT-TDP and then applying repeated vacuum/N_2 cycles.[52,60] Following centrifugation and multiple washing cycles of the retrieved pellets, we noted a consistent shift in colour from the original white of the pristine HNT or HNT-TDP to the specific colours as shown in the sunlight digital images of the samples in Fig. S2.† Additionally, all the samples treated with the two porphyrins exhibited luminescence under UV lamp irradiation.

We also prepared two ground samples by grinding pristine HNT with either H_2TPPF_{20} or $ZnTPPF_{20}$.

To determine whether the porphyrins were loaded into the HNT lumen or merely interacting with the external surface of the nanotubes, we conducted an extensive spectroscopic analysis of all the samples. Although FTIR spectroscopy did not provide conclusive information (see the ESI, Fig. S3 and S4†), DRS and solid state emission spectroscopy as well as TEM microscopy were employed to detect and localize the porphyrin molecules.

2.3 HNT-covering by dextrin

To avoid the burst release of the porphyrins in the very first few minutes after suspending the HNT-composites in water and to improve the suspendibility of the nanotubes in water, we carried out a covering step on loaded samples. To do that, we used the pH-sensitive polymer dextrin by following a procedure already described in the literature (see the Experimental part).[60,61] The success of the HNT covering process with dextrin was assessed by TGA (see below), while by TEM, the polymer was not easily detectable because of its very poor contrast. Nevertheless, a careful comparison of the images of the untreated (Fig. S5†) and treated HNT helped in tentatively recognizing the dextrin cap (highlighted with red arrows in Fig. S5†) at the entrance of the HNT tubes as a curved light-grey layer. Moreover, we verified by SEM (Fig. S6†) that the dextrin coating extends over the entire HNT surface and appears on the nanotube openings as well, albeit to a minor extent compared to that observed in other literature reports, where only the capping of the nanotube entrances was visible.[60,61] In addition, TEM micrographs showed the presence of porphyrins in the inner lumen as light-grey bubble-like structures attributed to the drug loading in other literature papers.[60] Unfortunately, attempts to localize the porphyrins at the nanoscale level by mapping fluorine atoms of the porphyrins by energy dispersive X-ray spectroscopy (EDS) did not give any reliable information because the fluorine signal was too weak. To confirm that the major amount of porphyrins was located in the inner lumen, we investigated the samples with UV-vis and emission spectroscopy.

2.4 Diffuse reflectance spectroscopy

DRS was employed to characterize the HNT–porphyrin composites in their solid state. This technique aimed to provide insights into the location of the porphyrins and their aggregation state through absorption spectroscopy. The comprehensive spectra for H_2TPPF_{20}- and $ZnTPPF_{20}$-based derivatives are shown in Fig. S7,† while Fig. 3a and b provide focused views of their UV-vis regions, spanning from 190 to 800 nm. Both pristine HNT and HNT-TDP (depicted, respectively, as light-blue and yellow traces in Fig. 3) exhibit a notable absorption peak in the UV region at 255 nm, characteristic of such inorganic oxide matrices.[62]

Moreover, the complete DRS spectra, recorded up to 2600 nm (Fig. S7†), also showed three typical peaks at 1408 nm, 1920 nm, and 2208 nm attributed to water,[63] possibly present externally, internally and in the interlayer districts. In the same region, and only for the TDP-containing samples, a band peaking at 1733 nm was visible and thus attributed to TDP by direct comparison. Focusing on the visible range, the typical electronic transitions of porphyrin structures clearly emerged. H_2TPPF_{20} and $ZnTPPF_{20}$ exhibited the characteristic B and Q bands of porphyrins,[64–66] which are recognizable in all four loaded samples. The H_2TPPF_{20} DRS spectrum (Fig. 3a, black trace) recalls the typical pattern of a free-base porphyrin, with a B band at 419 nm ($S_0 \rightarrow S_2$ transition) and four weaker Q-bands at 505, 538, 582 and 636 nm ($S_0 \rightarrow S_1$ transitions, see Table 2). The comparison of the DRS spectrum of the solid with the one of H_2TPPF_{20} recorded in THF solution (410, 504, 534, 582 and 657 nm, Fig. S7a†) shows a 9 nm red shift of the B band and a 21 nm blue-shift of the last Q band. The bathochromic shift observed in the B band, coupled with the broad absorption bands, is rationally attributed to the π–π stacking interactions between the porphyrin cores, thus indicating the presence of aggregates in the solid state (see also Fig. S7c† and the associated comment). These spectral features, as expected, are also notice-

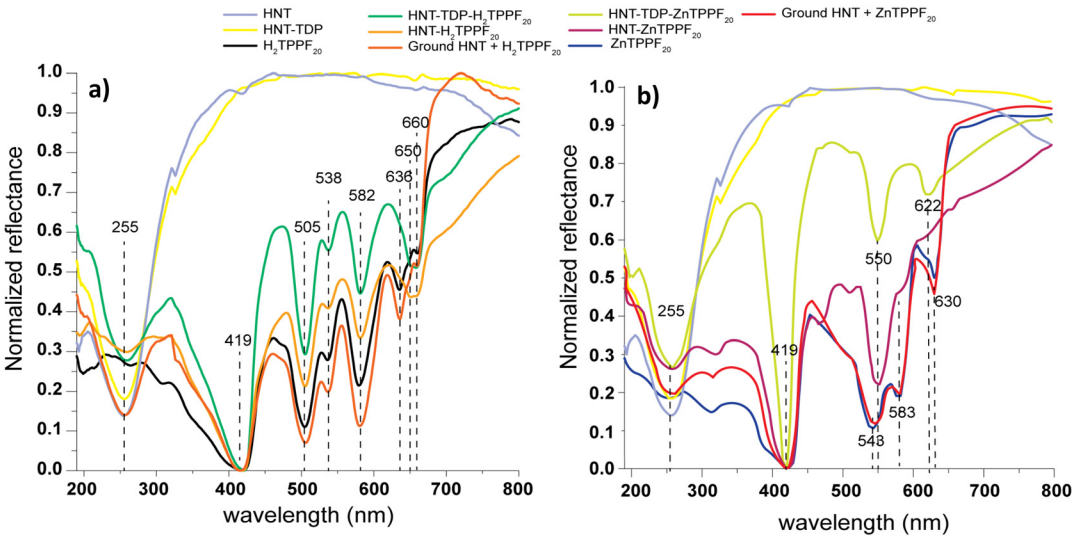

Fig. 3 DRS spectra of pristine halloysite and HNT modified with TDP, loaded with H_2TPPF_{20} (panel a) and $ZnTPPF_{20}$ (panel b). Black and blue traces are the spectra of H_2TPPF_{20} and $ZnTPPF_{20}$, respectively, diluted with $BaSO_4$.

Table 2 Photophysical data in the solid state of all the compounds and composites studied. For comparison, data of H_2TPPF_{20} and $ZnTPPF_{20}$ in THF solution are also reported

	Absorption (λ, nm)		Emission (λ, nm)
Entry	B band	Q bands	Q bands
H_2TPPF_{20} in THF	*410*	*504, 534, 582, 657*	*639, 659, 690 (sh), 706*
H_2TPPF_{20} in THF : H_2O 20 : 80	*412*	*505, 535, 582, 657*	*664, 706*
H_2TPPF_{20}	419	505, 538, 582, 636	663, 706
Ground HNT + H_2TPPF_{20}	419	505, 538, 582, 636	663, 706
HNT-H_2TPPF_{20}	419	505, 538, 582, 650	663, 706
HNT-TDP-H_2TPPF_{20}	419	505, 538, 582, 650	663, 706
Zn-$TPPF_{20}$ in THF	*419*	*550, 585*	*589, 644*
Zn-$TPPF_{20}$ in THF : H_2O 20 : 80	*421*	*550, 585*	*589, 633 (sh), 644*
Zn-$TPPF_{20}$	419	500 (sh), 548, 583, 630	633, 690
Ground HNT + $ZnTPPF_{20}$	419	500 (sh), 548, 583, 630	633, 700
HNT-Zn-$TPPF_{20}$	419	510, 550, 583 (sh), 622	589 (sh), 654, 704 (sh)
HNT-TDP-$ZnTPPF_{20}$	419	550, 622	589 (sh), 654

able in the ground HNT + H_2TPPF_{20} sample. By moving to the loaded samples HNT-H_2TPPF_{20} (light orange trace, Fig. 3a) and HNT-TDP-H_2TPPF_{20} (green trace, Fig. 3a), a progressive sharpening of the absorption bands can be observed, especially for the TDP-based composite, along with a shift of the lowest energy Q band (650 nm), similar to the porphyrin in solution. This similarity to the spectrum of the porphyrin in solution, where it exists in the monomer form, suggests that the molecules in the loaded samples are more dispersed than in the pristine solid, while still retaining some degree of aggregation, as confirmed by the emission spectra (see section 2.5). Indeed, the spectrum of the ground HNT + H_2TPPF_{20} sample resembles that of pure H_2TPPF_{20} with the last Q band again appearing at 636 nm. In other words, a clear bathochromic shift of the lowest-energy Q band is observable in the DRS spectra of the loaded samples, compared to those of pristine H_2TPPF_{20} and the HNT + H_2TPPF_{20} ground samples, indicating a higher degree of dispersion in the former.

Moving from H_2TPPF_{20} to $ZnTPPF_{20}$, the ring symmetry of the planar macrocycle increases from D_{2h} to D_{4h}, simplifying the solution spectrum to exhibit a B band at 419 nm and only two Q bands at 550 and 585 nm (Fig. S8b†). In its solid form, interactions among the stacked porphyrin cores can result not only in broader absorption bands but also in a more complex absorption pattern. As a proof of concept, in addition to the broadening of the B band (419 nm) and the two Q bands centered at 548 and 583 nm, the $ZnTPPF_{20}$ DRS spectrum shows multiple transitions, with a shoulder around 500 nm and an additional vibronic band at 630 nm being particularly evident (Fig. 3b). As expected, the DRS spectrum of the ground HNT + $ZnTPPF_{20}$ sample is superimposable with that of $ZnTPPF_{20}$, while the two loaded samples show a significant sharpening

and a simplification of the absorption pattern, resembling that of single molecules recorded in solution. However, some differences can be noted when focusing on Q-bands; the Q transitions at higher energies (*ca.* 550 nm) become narrower as the samples shift from aggregates to more dispersed forms (see also Fig. S8d† for the B band). In the case of HNT-TDP-ZnTPPF$_{20}$, only the Q band at 550 nm is perceivable, similar to the one observed for ZnTPPF$_{20}$ in THF solution (Fig. S8b†). The Q transition at 583 nm gradually decreases in loaded samples, as evidenced by only a shoulder being discernible in HNT-ZnTPPF$_{20}$, which completely disappears in HNT-TDP-ZnTPPF$_{20}$ (Fig. 3b). Conversely, the additional Q transition at lower energies (>600 nm), which emerged in the solid state, remains visible in all DRS spectra and appears blue-shifted (622 nm) in the most dispersed sample (HNT-TDP-ZnTPPF$_{20}$), attributed to the interaction of the porphyrin molecules with the TDP environment.

In summary, DRS shows that in both free-base and zinc porphyrins, whether as pristine solids or ground samples with HNT, the absorption spectra exhibit more complex patterns and broadened bands, as expected from aggregated solid states. Conversely, the loaded samples exhibit absorption patterns resembling those recorded in THF solution, indicating that the PS molecules are more dispersed in the matrix. It is worth noting that this behavior is more pronounced in TDP-functionalized HNT samples, particularly for Zn-TPPF$_{20}$ loaded samples.

2.5 Solid-state photoluminescence spectroscopy

To gain insight into the primary location of porphyrins within HNT, we also employed photoluminescence spectroscopy. We first recorded the spectra of H$_2$TPPF$_{20}$ and Zn-TPPF$_{20}$ in diluted THF solution, where only single molecules are present.[67] Then, we moved to diluted THF/H$_2$O 2 : 8 mixtures, where some aggregation is expected to occur,[67] and finally to the solid state, where aggregation is prevalent. This approach allowed us to reasonably evaluate the emission properties of plain H$_2$TPPF$_{20}$ and ZnTPPF$_{20}$ in different aggregation states. Subsequently, we measured the emission profiles for all the loaded and ground samples. Fig. 4a presents a synopsis of all the normalized emission spectra, and Table 2 presents all the corresponding data. It is worth noting that the emission spectra of all the samples exciting at three distinct wavelengths were acquired, and in any case, the emission was independent of the excitation wavelength, as expected according to Kasha's rule (Fig. S9†).

The THF spectrum of H$_2$TPPF$_{20}$ shows three main emission bands centred at 639, 659 and 706 nm, with a slightly perceivable shoulder at *ca.* 690 nm. Upon increasing the amount of a non-solvent, such as water, while keeping the concentration constant until reaching a THF/H$_2$O ratio of 2 : 8, the spectrum changes significantly. The transitions at 639 nm are almost completely quenched, while the middle transition remains visible but is slightly red-shifted at 664 nm, and the 706 nm

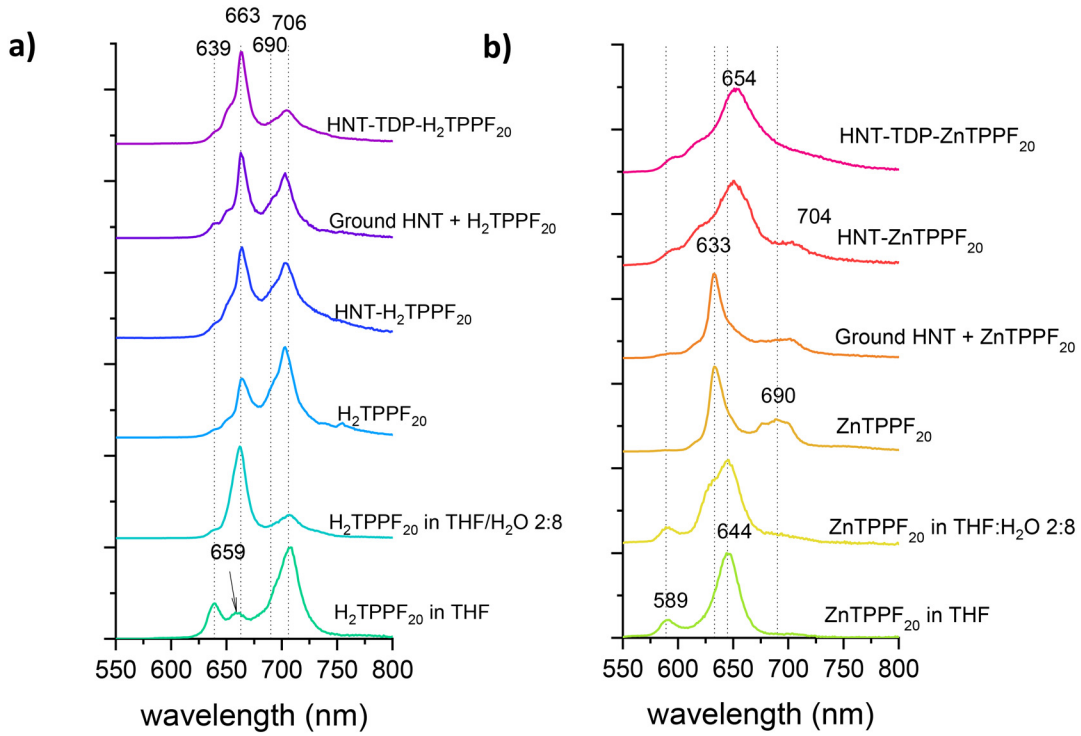

Fig. 4 Stacked plot of the normalized emission spectra of (a) H$_2$TPPF$_{20}$ in THF solution, H$_2$TPPF$_{20}$ in THF/H$_2$O 2 : 8 solution, H$_2$TPPF$_{20}$ alone, loaded HNT-H$_2$TPPF$_{20}$, ground HNT + H$_2$TPPF$_{20}$ and HNT-TDP-H$_2$TPPF$_{20}$; and (b) ZnTPPF$_{20}$ in THF solution, ZnTPPF$_{20}$ in THF/H$_2$O 2 : 8 solution, ZnTPPF$_{20}$ alone, loaded HNT-ZnTPPF$_{20}$, ground HNT + ZnTPPF$_{20}$ and HNT-TDP-ZnTPPF$_{20}$.

band is greatly reduced. This significant change in the emission profile, in accordance with the literature,[67] can be ascribed to micro-aggregation processes towards the formation of J-aggregates.

The emission profile of solid H_2TPPF_{20} retains the Q band at 663 nm, along with a dominant transition at 706 nm. The spectra of loaded H_2TPPF_{20} and ground HNT + H_2TPPF_{20} resemble that of pristine H_2TPPF_{20}, whereas in the presence of TDP, the band at 706 nm significantly decreases, and the spectral pattern becomes almost superimposable to that of H_2TPPF_{20} in a THF/H_2O 2 : 8 mixture.

Therefore, the photoluminescence investigation of H_2TPPF_{20} and the corresponding hybrids supports the suggestions of a higher degree of dispersion of H_2TPPF_{20} when loaded onto TDP-modified HNT, as indicated by DRS spectra. Conversely, the loaded HNT-H_2TPPF_{20} shows an emission pattern very similar to that of pristine H_2TPPF_{20} and the ground HNT + H_2TPPF_{20} samples, where extended aggregates are present (Fig. 4a).

The emission spectrum of $ZnTPPF_{20}$ in THF shows a very low Q band at 589 nm and an intense Q band at 644 nm (Fig. 4b). Upon addition of water, a shoulder at 633 nm appears, which can reasonably be attributed to the presence of small aggregates, as it becomes the predominant transition in the spectrum of solid $ZnTPPF_{20}$, where aggregation is more likely. Not surprisingly, this band also prevails in the spectrum of ground HNT + $ZnTPPF_{20}$, which is almost superimposable to that of the plain solid sample. Conversely, when $ZnTPPF_{20}$ is loaded onto HNT, and more evidently when HNT is functionalized with TDP, the emission profile changes significantly, featuring a very broad and red-shifted band at 654 nm. In HNT-$ZnTPPF_{20}$, this band is accompanied by a second, less-pronounced band at lower energy (704 nm), which is no longer present in HNT-TDP-$ZnTPPF_{20}$. In addition, in both loaded samples, a shoulder at *ca.* 589 nm becomes noticeable, corresponding to the lower-energy Q transition in the $ZnTPPF_{20}$ spectra in THF and THF/H_2O solutions. Notably, this band is absent in both pristine $ZnTPPF_{20}$ and ground HNT + $ZnTPPF_{20}$ spectra, suggesting a more dispersed condition in loaded samples.

In summary, the photoluminescence study further confirms the DRS findings, indicating that the loaded samples closely resemble the solution state, which is characterized by a lower degree of aggregation, especially for $ZnTPPF_{20}$ and when TDP is present in the inner lumen of HNT.

2.6 TGA

The loading percentage of H_2TPPF_{20} and $ZnTPPF_{20}$ was estimated through TG-DTG analysis under an air flux, comparing the TG-DTG profiles of pristine HNT and H_2TPPF_{20} and $ZnTPPF_{20}$ alone with those of the ground and loaded samples. The results are summarized in Table 3.

The pristine HNT typically show a step in the TG profile characterized by an onset temperature (T_{onset}) at *ca.* 450 °C and an inflection point at 495 °C, usually accounting for a weight loss of *ca.* 12% (Fig. S10a†). This step is present in all the TGA profiles of the investigated samples. The TGA profiles of the ground samples show further weight loss steps at lower temperatures (T_{onset} *ca.* 350 °C, inflection point = 373–375 °C) (Fig. S11a and S11b†). Since H_2TPPF_{20} and $ZnTPPF_{20}$ alone show a weight loss step at 415 (Fig. S10b†) and 425 °C (Fig. S10c†), respectively, we attributed the loss steps to a thermo-oxidative degradation of the two porphyrins catalyzed by the outer surface of HNT. On moving from physically mixed ground to loaded samples (Fig. S11c and S11d†), the DTG profile reveals a small peak significantly shifted towards lower temperatures, which is attributed to a very small amount of porphyrins present on the HNT outer surface. On the other hand, in the TGA profile of the loaded HNT-H_2TPPF_{20} sample (Fig. S11c†), a shoulder with an inflection point at 448 °C and superimposed to the HNT dehydroxylation is visible. This evidence, together with the weight loss step value, which accounts for more than what expected for the HNT dehydroxylation alone, suggests the presence of the major part of H_2TPPF_{20} located in the inner lumen. Indeed, it is known that organic molecules in the inner lumen of HNT usually strongly increase their degradation temperature due to the entrapment into the nanotube cavity,[68] thus supporting the inner location hypothesis, already suggested by the spectroscopic data.

Regarding the TDP-containing samples, the TG profiles (Fig. S11e and S11f†) show an overlap between the weight loss step due to TDP oxidation (Fig. S12†) and those of the porphyrins.

In the case of the dextrin-covered samples (Fig. S11g–j†), the peaks at *ca.* 265 °C in the DTGA profiles account for the contribution of dextrin.

We tentatively estimated the loading efficiency percentage of H_2TPPF_{20} and $ZnTPPF_{20}$ on pristine and TDP-modified HNT by calculating the ratio of the mass percentage loss obtained from TGA, attributed to the actual PS loading, and the maximum theoretical mass percentage of porphyrin loadable in the inner lumen (6.2%), based on geometric considerations. This calculation considered a mean inner lumen diameter of 15 nm, a mean outer diameter of 50 nm, the density of HNT (2.53 g cm^{-3}),[13] and the density of porphyrin (1.7 g cm^{-3}),[69] as detailed in the ESI.† At the same time, due to the overlap in the loss steps of several components, the real mass percentage PS loading was evaluated by subtracting the OH dehydroxylation

Table 3 Drug content weight % estimated through TGA-DTGA for the different loaded samples. TDP amount is always equal to 5%, as measured on the precursor HNT-TDP (see Fig. S12 of the ESI†). The loading efficiency % is reported in the last column

Sample content	PS %w	PS loading efficiency %w
HNT-H_2TPPF_{20}	4.2	68
HNT-TDP-H_2TPPF_{20}	6.2	>98
HNT-H_2TPPF_{20}-Dextrin	3.3	53
HNT-TDP-H_2TPPF_{20}-Dextrin	5.9	95
HNT-Zn-$TPPF_{20}$	1.2	19
HNT-TDP-$ZnTPPF_{20}$	2.4	39
HNT-$ZnTPPF_{20}$-Dextrin	0.7	11
HNT-TDP-$ZnTPPF_{20}$-Dextrin	0.4	6

contribution (*ca.* 12%) to the whole TG step. Additionally, in relation to the HNT-TDP samples, due to the overlap in the degradation range of porphyrins and TDP (compare Fig. S11 and S12†), we quantified the loaded porphyrins by subtracting also the amount of TDP determined in the HNT-TDP precursor (5%, Fig. S12†). This approach yielded the data reported in Table 3.

A significant increase in PS loading efficiencies is observed for both porphyrins when HNT are functionalized with TDP (68% *vs.* 98% for H_2TPPF_{20} and 19% *vs.* 39% for $ZnTPPF_{20}$). This is consistent with the possibility of hydrophobic interactions between the apolar TDP tails and the perfluorinated macrocycles, considering the well-known hydrophobicity of fluorine atoms. In addition, since TDP is selectively anchored to the inner lumen,[10,53,54] this result may suggest a preferential inner lumen location for the porphyrins.

For the dextrin-covered samples, the weight percentages of H_2TPPF_{20} and $ZnTPPF_{20}$ decrease compared to their corresponding precursors. We attribute this to the capping process (see the experimental part), during which some release from the HNT lumen may occur. This is particularly evident in the case of $ZnTPPF_{20}$.

Overall, the PS loading efficiencies of $ZnTPPF_{20}$-containing samples are lower than those of H_2TPPF_{20} samples, both in pristine and functionalized HNT. This may be due to the loading procedure (see the experimental part), which involves prolonged stirring in THF, potentially enhancing the release of $ZnTPPF_{20}$ compared to H_2TPPF_{20}, as zinc can axially coordinate with the solvent. Additionally, the lower uptake of $ZnTPPF_{20}$-containing samples combined with the effect of TDP functionalization, may reasonably explain the absorption pattern, which is more similar to that of a single molecule in solution.

2.7 Porphyrin release study

The slow release of the PS (H_2TPPF_{20} and Zn-$TPPF_{20}$) loaded within the HNT composites was investigated in a 1 : 1 THF : H_2O mixture using UV-vis spectroscopy.

Fig. S13† illustrates the setup used for the time-based release analysis, which involved the following: (i) cycles of stirring, (ii) centrifugation to retrieve the HNT, and (iii) separation of HNT from the supernatant to prevent HNT scattering during UV-vis analysis and stop the release process. Fig. 5 presents the drug release profiles of HNT, both before and after treatment with dextrin.

The experimental points of the release profiles were best fitted using the sum of two first-order kinetics[70] (eqn (2)):

$$R = M_1(1 - e^{-k_1 * t}) + M_2(1 - e^{-k_2 * t}) \quad (2)$$

where M is the amount of active agent released at a specific time, and k is the release rate constant. This provided insights into the release kinetics, suggesting the presence of two distinct release sites.

For all samples, there is an initial burst release within the first 15 minutes, which is still much slower than that of the ground sample (star symbols in Fig. 5). This burst release can be ascribed either to traces of porphyrin on the outer surface or

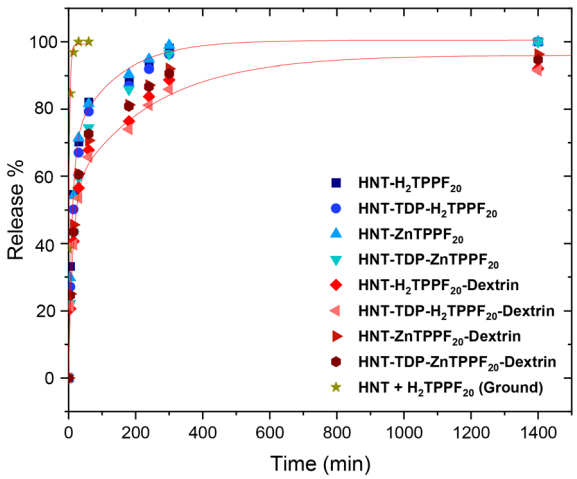

Fig. 5 Release of H_2TPPF_{20} and $ZnTPPF_{20}$ from the loaded HNT samples both before and after treatment with dextrin.

to the fraction contained within the very short HNT component of the commercial HNT used in this work, which, as revealed by TEM images, is significantly polydispersed. Instead, the other slower kinetic regime can be attributed to the release of porphyrins from the inner part of the longer HNT component.

By taking into account the fact that there may be several parameters affecting the release dynamics (the PS affinity for the solvent, the effective PS loading, the specific PS distribution within the inner lumen), we did not encounter any significant release ability variation among the investigated uncovered samples. Interestingly, the dextrin covering produced a slight but noticeable slowing down of the release, also allowing a better nanotube suspension in aqueous solutions for a much longer time when not shaken. A further slight slowing of the release process is attained by combining the dextrin covering with TDP modification, possibly owing to the weak hydrophobic interactions between the apolar porphyrin and the TDP tails in the inner lumen.

2.8 Fluorescence microscopy and PDT treatment on three different tumor cell lines

Three different tumor cell lines were selected to test the ability of HNT to enter cells and to assess the capacity of the perfluorinated porphyrin to induce cell death upon irradiation with visible light. In particular, we selected three cell lines including one prostate cancer (PC3) and two bladder cancer (5637 and UMUC3) lines resembling different grades and stages of the disease. The HNT-TDP-H_2TPPF_{20}-Dextrin sample was selected among the others, as it contained one of the highest amounts of porphyrin (Table 3) and exhibited the slowest release kinetic profile (light red triangle, Fig. 5).

The kinetic uptake of HNT was studied by incubating PC3, 5637 and UMUC3 cells with 10 μg mL^{-1} HNT for 4 and 24 hours. Reflected light microscopy, which does not require fluorescence labelling to obtain a signal for confocal microscopy, was used for this analysis. The assay was carried

out after the nuclei and cytoskeleton were immunostained with Hoechst and phalloidin, respectively, revealing that accumulation at the cellular level became easily observable after 24 hours (Fig. S14†). Fig. S15–S17† show fluorescence and reflectance images (*z*-stack) for the three cell lines studied. No significant differences in internalization were observed among the cell lines; in all cases, HNT appeared to accumulate at the cytosol level.

Similar samples were prepared by incubating HNT-TDP-H_2TPPF_{20}-Dextrin for 24 hours and performing immunostaining only with phalloidin, as the emission tail from Hoechst interfered with the porphyrin emission in the red channel. In these samples, it is clearly observed that the emission signal is effectively co-localized with the reflectance signal, corresponding to the HNT (Fig. 6).

Cell viability was then measured by MTT tests on all the three tumor cell lines after incubating them for 24 hours with both pristine HNT and loaded HNT-TDP-H_2TPPF_{20}-Dextrin at different concentrations in the range of 0.01–100 μg mL^{-1}. Pristine HNT showed the same non-toxic behavior in the dark until a dose of 10 μg mL^{-1} HNT, while 5637 and UMUC3 cells showed a small dark cytotoxicity. Under irradiation for 45 minutes with a led lamp (1.3 mW cm^{-2} in the 400–800 nm range, emission profile reported in Fig. S18†), a certain difference in cytotoxicity was noted between the three distinct cell lines. In particular, 5637 cells revealed to be more sensitive to HNT presence, exhibiting a consistent reduction of viability even at lower HNT concentrations and showing a small difference in cell viability under irradiation compared to the dark conditions (Fig. 7, panels A). This is not unusual and some of us have already observed different sensitivities, with 5637 more sensitive than UMUC3 cells.[71]

By comparing the toxicity capabilities of HNT and porphyrin-loaded HNT under irradiation, we can clearly observe the role played by H_2TPPF_{20} in favouring the singlet oxygen production, thus inducing an overall higher toxicity, especially at the highest dose (100 μg mL^{-1}) for PC3 and UMUC3 cells. Similar to the response towards HNT, even towards porphyrin, 5637 cells showed to be more sensitive than the other two cell types and, in this case, a significant reduction of cell viability was detected for doses >1 μg mL^{-1} (Fig. 7, panels C). Finally, the comparison of cell viability curves in the dark and after light irradiation of cells treated with HNT-TDP-H_2TPPF_{20}-Dextrin (Fig. 7, panels B) led us to estimate the EC_{50} values, which represent the effective concentration required to reduce cell viability to 50% in the dark and after irradiation, respectively (see Table 4).

These preliminary data confirm a cytotoxic effect of the investigated nanocomposites, which is enhanced when the cells are exposed to irradiation, thus underscoring the critical role of the photosensitizer.

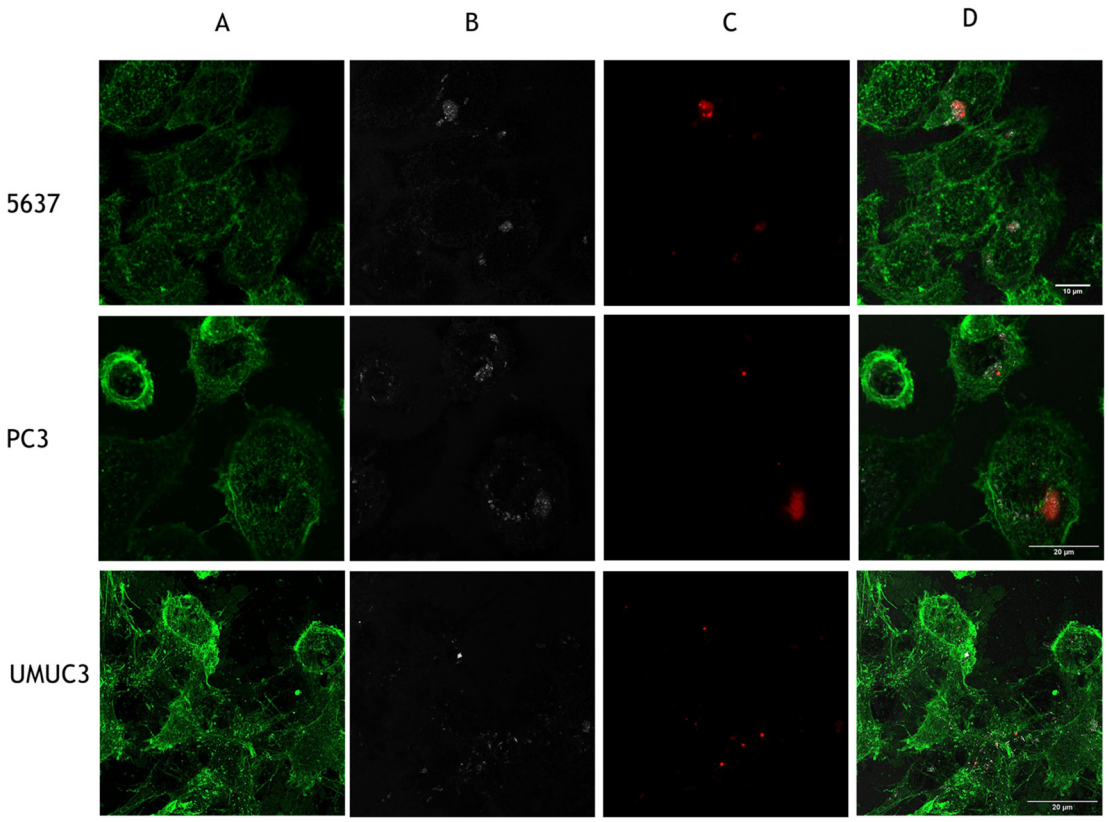

Fig. 6 Confocal microscopy images of 5637, PC3, and UMUC3 cells treated with HNT-TDP-H_2TPPF_{20}-Dextrin for 24 hours. (A) Phalloidin fluorescence (green) visualizing the cytoskeleton; (B) reflected light (white) localizing the HNT; (C) porphyrin fluorescence (red); and (D) superposition of the three channels. All the images are the superposition of several images acquired along the optical axis (*z*-stack).

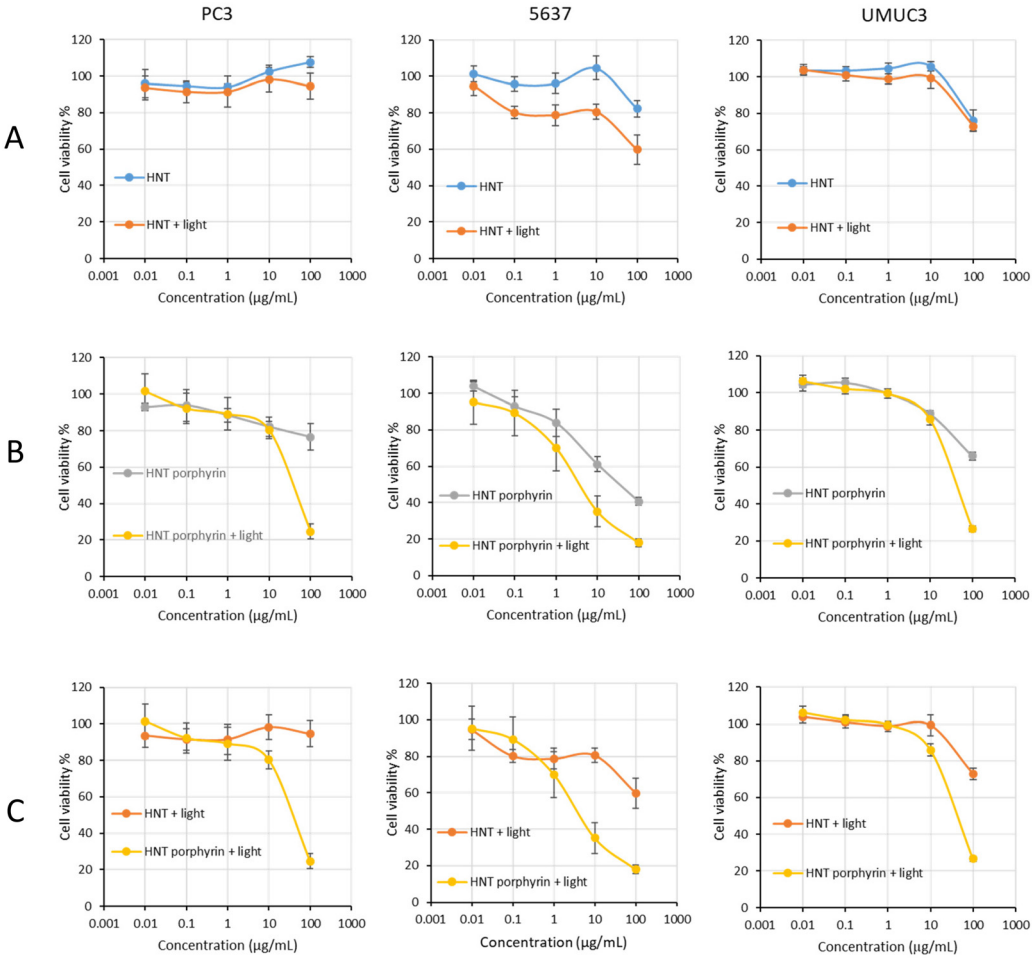

Fig. 7 Dose–response plots for pristine and loaded HNT (HNT-TDP-H_2TPPF_{20}-Dextrin) in the dark and under visible light irradiation (irradiation time = 45 min). Panel A: cell viability after treatment with pristine HNT in the dark and under light irradiation. Panels B: cell viability after treatment with loaded HNT in the dark and under light irradiation. Panels C: cell viability after treatment with pristine and loaded HNT, both under light irradiation.

Table 4 Cytotoxicity of the HNT-TDP-H_2TPPF_{20}-dextrin nanocomposite on PC3, 5637, and UMUC3 cells in the dark and upon irradiation, expressed in terms of dark EC_{50} and light EC_{50}. PI is the phototherapeutic index and is defined as the ratio of dark-EC_{50}/light-EC_{50}

Cells	Dark EC_{50}	Light EC_{50}	PI
PC3	>100 μg mL^{-1}	50 μg mL^{-1}	>2
5637	35 μg mL^{-1}	3.5 μg mL^{-1}	10
UMUC3	>100 μg mL^{-1}	50 μg mL^{-1}	>2

3. Conclusions

In the present work, we developed and characterized HNT-based molecular nanocarriers for potential PDT applications, combining the two perfluorinated porphyrins, H_2TPPF_{20} and $ZnTPPF_{20}$, with pristine or TDP-modified HNT. The well-established ability to react with O_2 and generate cytotoxic singlet oxygen species for PDT treatment of porphyrin-based photosensitizers was ascertained in a polar solvent such as ethanol, where the perfluorinated porphyrins even with a certain degree of aggregation were still able to produce $^1O_2$. TDP was selected to create an appropriate apolar environment within the lumen of HNT, facilitating the loading of fluorinated lipophilic photosensitizers into the carrier. The dextrin covering process was carried out on the loaded samples to better suspend HNT in water media and slightly delay the release of guest molecules from the nano-carriers. To validate our approach, we thoroughly examined the spectroscopic and thermogravimetric properties of the loaded samples, both with and without dextrin. We also studied H_2TPPF_{20} and $ZnTPPF_{20}$ in their pristine form and mechanically mixed with HNT, as any interaction in the ground samples would only occur with the silica-based external part of the nanoclay. This comprehensive study provided valuable insights into the impact of HNT modification on the location, loading efficiency and release of the perfluorinated porphyrins.

A combination of ATR-FTIR, DRS, and solid-state emission spectroscopy provided insights into the aggregation and dispersion state of the PS, as well as their interactions with the different environments created by the derivatized and non-derivatized carriers. The observations showed that in the loaded samples, the PS molecules appeared dispersed as they were in solution, particularly when HNT were selectively functionalized in the inner lumen with apolar TDP. This was further supported by solid-state emission spectroscopy, which also demonstrated a solution-like situation for the loaded samples, especially for the HNT-TDP-ZnTPPF$_{20}$ sample.

The beneficial effect of TDP functionalization on PS uptake into HNT was demonstrated by TGA, which revealed a significant increase in loading efficiencies for both free-base and zinc porphyrins. Our findings suggest that the porphyrins preferentially locate in the inner lumen of HNT, where TDP is selectively anchored, exposing the hydrophobic tails.

We have demonstrated the potential of porphyrin-loaded HNT in the context of cancer by assessing their impact on tumor cells. Upon internalization, they significantly reduced the viability of all the cell lines tested and the effect is more consistent upon irradiation, indicating the efficacy of the photosensitizer responsible for singlet oxygen generation.

Additionally, we plan to explore whether these adducts can function as ^{19}F-based MRI contrast agents.[72] This development could transform the nanohybrids into theranostic probes, combining luminescence properties for photodynamic therapy and fluorescence imaging with ^{19}F magnetic features for *in vivo* tracking.

Author contributions

Hady Hamza: investigation, writing – original draft, and methodology; Veronica Schifano: investigation, writing – review & editing, and validation; Giorgia Colciago: investigation and methodology; Marco Aldo Ortenzi: investigation and writing – review & editing; Anna Maria Ferretti: methodology and writing – review & editing; Gabriele Di Carlo: writing – review & editing and resources; Maria Vittoria Dozzi: methodology and writing – review & editing; Riccardo Vago: writing – review & editing and resources; Francesca Tessore: writing – review & editing, investigation, and resources; and Daniela Maggioni: conceptualization, writing – original draft, investigation, writing – review & editing, supervision, methodology, project administration, and resources.

Conflicts of interest

There are no conflicts to declare.

Data availability

The data supporting this article have been included as part of the ESI.†

Acknowledgements

This work was supported by the Università degli Studi di Milano (project PSR2022_DIP_005_PI_LCARL). The use of equipment purchased through the Regione Lombardia–Fondazione Cariplo joint SmartMatLab Project (2013-1766) is gratefully acknowledged. Part of this work was carried out at NOLIMITS, an advanced imaging facility established by the Università degli Studi di Milano. D. M. and F. T. warmly thank Prof. Silvia Bruni for her helpful discussion.

References

1 M. Izci, C. Maksoudian, B. B. Manshian and S. J. Soenen, *Chem. Rev.*, 2021, **121**, 1746–1803.
2 Y. Feng, X. Chen, R.-R. He, Z. Liu, Y. M. Lvov and M. Liu, *ACS Nano*, 2024, **18**, 20001–20026.
3 I. R. Wilson, *Clay Miner.*, 2004, **39**, 1–15.
4 I. R. Wilson, H. de Souza Santos and P. de Souza Santos, *Clay Miner.*, 2006, **41**, 697–716.
5 E. Joussein, S. Petit, J. Churchman, B. Theng, D. Righi and B. Delvaux, *Clay Miner.*, 2005, **40**, 383–426.
6 P. Yuan, D. Tan and F. Annabi-Bergaya, *Appl. Clay Sci.*, 2015, **112–113**, 75–93.
7 V. Vergaro, E. Abdullayev, Y. M. Lvov, A. Zeitoun, R. Cingolani, R. Rinaldi and S. Leporatti, *Biomacromolecules*, 2010, **11**, 820–826.
8 H. Zhang, *Nanotechnol. Rev.*, 2017, **6**, 573–581.
9 M. Massaro, G. Cavallaro, C. G. Colletti, G. Lazzara, S. Milioto, R. Noto and S. Riela, *J. Mater. Chem. B*, 2018, **6**, 3415–3433.
10 T. Taroni, D. Meroni, K. Fidecka, D. Maggioni, M. Longhi and S. Ardizzone, *Appl. Surf. Sci.*, 2019, **486**, 466–473.
11 J. Liao, H. Wang, N. Liu and H. Yang, *Adv. Colloid Interface Sci.*, 2023, **311**, 102812.
12 G. Biddeci, G. Spinelli, P. Colomba and F. Di Blasi, *Int. J. Mol. Sci.*, 2022, **23**, 11518.
13 Y. Lvov, W. Wang, L. Zhang and R. Fakhrullin, *Adv. Mater.*, 2016, **28**, 1227–1250.
14 S. Satish, M. Tharmavaram and D. Rawtani, *Nano Biomed.*, 2019, **6**, 1–16.
15 Y. Lee, G.-E. Jung, S. J. Cho, K. E. Geckeler and H. Fuchs, *Nanoscale*, 2013, **5**, 8577–8585.
16 J. Tully, R. Yendluri and Y. Lvov, *Biomacromolecules*, 2016, **17**, 615–621.
17 H. Lun, J. Ouyang and H. Yang, *RSC Adv.*, 2014, **4**, 44197–44202.
18 G. Y. Kırımlıoğlu and Y. Yazan, *Eur. Int. J. Sci. Technol.*, 2016, **5**, 99–109.
19 Z. Long, J. Zhang, Y. Shen, C. Zhou and M. Liu, *Mater. Sci. Eng., C*, 2017, **81**, 224–235.
20 Y.-F. Shi, Z. Tian, Y. Zhang, H.-B. Shen and N.-Q. Jia, *Nanoscale Res. Lett.*, 2011, **6**, 608.
21 Y. M. Lvov, M. M. DeVilliers and R. F. Fakhrullin, *Expert Opin. Drug Delivery*, 2016, **13**, 977–986.

22 Y. Lvov and E. Abdullayev, *Prog. Polym. Sci.*, 2013, **38**, 1690–1719.
23 M. Massaro, R. Amorati, G. Cavallaro, S. Guernelli, G. Lazzara, S. Milioto, R. Noto, P. Poma and S. Riela, *Colloids Surf., B*, 2016, **140**, 505–513.
24 M. Massaro, R. Noto and S. Riela, *Molecules*, 2020, **25**, 4863.
25 N. P. Truong, M. R. Whittaker, C. W. Mak and T. P. Davis, *Expert Opin. Drug Delivery*, 2015, **12**, 129–142.
26 V. P. Chauhan, Z. Popović, O. Chen, J. Cui, D. Fukumura, M. G. Bawendi and R. K. Jain, *Angew. Chem., Int. Ed.*, 2011, **50**, 11417–11420.
27 T. I. Janjua, Y. Cao, C. Yu and A. Popat, *Nat. Rev. Mater.*, 2021, **6**, 1072–1074.
28 L. Gandarias and D. Faivre, *ChemPlusChem*, 2024, **89**(10), e202400090.
29 I. Pereira, M. Saleh, C. Nunes, S. Reis, F. Veiga and A. C. Paiva-Santos, *Adv. Colloid Interface Sci.*, 2021, **291**, 102406.
30 X. Zhao, J. Liu, J. Fan, H. Chao and X. Peng, *Chem. Soc. Rev.*, 2021, **50**, 4185–4219.
31 M. DeRosa, *Coord. Chem. Rev.*, 2002, **233–234**, 351–371.
32 H. Ding, H. Yu, Y. Dong, R. Tian, G. Huang, D. A. Boothman, B. D. Sumer and J. Gao, *J. Controlled Release*, 2011, **156**, 276–280.
33 L. Benov, *Med. Princ. Pract.*, 2015, **24**, 14–28.
34 S. Berardi, S. Caramori, E. Benazzi, N. Zabini, A. Niorettini, A. Orbelli Biroli, M. Pizzotti, F. Tessore and G. Di Carlo, *Appl. Sci.*, 2019, **9**, 2739.
35 F. Tessore, G. Di Carlo, A. Forni, S. Righetto, F. Limosani and A. Orbelli Biroli, *Inorganics*, 2020, **8**, 45.
36 G. Di Carlo, S. Caramori, L. Casarin, A. Orbelli Biroli, F. Tessore, R. Argazzi, A. Oriana, G. Cerullo, C. A. Bignozzi and M. Pizzotti, *J. Phys. Chem. C*, 2017, **121**, 18385–18400.
37 A. Orbelli Biroli, F. Tessore, M. Pizzotti, C. Biaggi, R. Ugo, S. Caramori, A. Aliprandi, C. A. Bignozzi, F. De Angelis, G. Giorgi, E. Licandro and E. Longhi, *J. Phys. Chem. C*, 2011, **115**, 23170–23182.
38 A. Orbelli Biroli, F. Tessore, G. Di Carlo, M. Pizzotti, E. Benazzi, F. Gentile, S. Berardi, C. A. Bignozzi, R. Argazzi, M. Natali, A. Sartorel and S. Caramori, *ACS Appl. Mater. Interfaces*, 2019, **11**, 32895–32908.
39 G. Di Carlo, C. Albanese, A. Molinari, S. Carli, R. Argazzi, A. Minguzzi, F. Tessore, E. Marchini and S. Caramori, *ACS Appl. Mater. Interfaces*, 2024, **16**, 14864–14882.
40 N. Tsolekile, S. Nelana and O. S. Oluwafemi, *Molecules*, 2019, **24**, 2669.
41 M. Ethirajan, Y. Chen, P. Joshi and R. K. Pandey, *Chem. Soc. Rev.*, 2011, **40**, 340–362.
42 L. N. Goswami, W. H. White, J. A. Spernyak, M. Ethirajan, Y. Chen, J. R. Missert, J. Morgan, R. Mazurchuk and R. K. Pandey, *Bioconjugate Chem.*, 2010, **21**, 816–827.
43 N. Bizaia, E. H. de Faria, G. P. Ricci, P. S. Calefi, E. J. Nassar, K. A. D. F. Castro, S. Nakagaki, K. J. Ciuffi, R. Trujillano, M. A. Vicente, A. Gil and S. A. Korili, *ACS Appl. Mater. Interfaces*, 2009, **1**, 2667–2678.
44 G. S. Machado, K. A. D. de Freitas Castro, F. Wypych and S. Nakagaki, *J. Mol. Catal. A: Chem.*, 2008, **283**, 99–107.
45 G. S. Machado, G. M. Ucoski, O. J. de Lima, K. J. Ciuffi, F. Wypych and S. Nakagaki, *Appl. Catal., A*, 2013, **460–461**, 124–131.
46 G. S. Machado, O. J. de Lima, K. J. Ciuffi, F. Wypych and S. Nakagaki, *Catal. Sci. Technol.*, 2013, **3**, 1094.
47 K. Teramura, K. Ogura, T. Sugimoto, H. Tsuneoka, T. Shishido and T. Tanaka, *Chem. Lett.*, 2009, **38**, 1098–1099.
48 S. Wei, Y. Yuan, W. Xie, J. Liao, R. Li, Y. Chen and H. Yang, *Small*, 2024, **20**(51), 2402648.
49 P. Foletto, F. Correa, L. Dornelles, B. A. Iglesias, C. H. da Silveira, P. A. Nogara, J. B. T. da Rocha, M. A. F. Faustino and O. E. D. Rodrigues, *Molecules*, 2018, **23**, 2588.
50 J. A. S. Cavaleiro, H. Görner, P. S. S. Lacerda, J. G. MacDonald, G. Mark, M. G. P. M. S. Neves, R. S. Nohr, H.-P. Schuchmann, C. von Sonntag and A. C. Tomé, *J. Photochem. Photobiol., A*, 2001, **144**, 131–140.
51 D. Samaroo, M. Vinodu, X. Chen and C. M. Drain, *J. Comb. Chem.*, 2007, **9**, 998–1011.
52 L. Lisuzzo, G. Cavallaro, P. Pasbakhsh, S. Milioto and G. Lazzara, *J. Colloid Interface Sci.*, 2019, **547**, 361–369.
53 H. Hamza, A. M. Ferretti, C. Innocenti, K. Fidecka, E. Licandro, C. Sangregorio and D. Maggioni, *Inorg. Chem.*, 2020, **59**, 12086–12096.
54 W. O. Yah, A. Takahara and Y. M. Lvov, *J. Am. Chem. Soc.*, 2012, **134**, 1853–1859.
55 Z. Liu, Y. Xue, M. Wu, G. Yang, M. Lan and W. Zhang, *Biomacromolecules*, 2019, **20**, 4563–4573.
56 S. Takizawa, R. Aboshi and S. Murata, *Photochem. Photobiol. Sci.*, 2011, **10**, 895–903.
57 D. Maggioni, M. Galli, L. D'Alfonso, D. Inverso, M. V. Dozzi, L. Sironi, M. Iannacone, M. Collini, P. Ferruti, E. Ranucci and G. D'Alfonso, *Inorg. Chem.*, 2015, **54**, 544–553.
58 L. Mascheroni, M. V. Dozzi, E. Ranucci, P. Ferruti, V. Francia, A. Salvati and D. Maggioni, *Inorg. Chem.*, 2019, **58**, 14586–14599.
59 H. Zhang, *Nanotechnol. Rev.*, 2017, **6**, 573–581.
60 M. R. Dzamukova, E. A. Naumenko, Y. M. Lvov and R. F. Fakhrullin, *Sci. Rep.*, 2015, **5**, 10560.
61 G. Fakhrullina, E. Khakimova, F. Akhatova, G. Lazzara, F. Parisi and R. Fakhrullin, *ACS Appl. Mater. Interfaces*, 2019, **11**, 23050–23064.
62 C. Li, J. Wang, S. Feng, Z. Yang and S. Ding, *J. Mater. Chem. A*, 2013, **1**, 8045–8054.
63 H.-D. Seelig, A. Hoehn, L. S. Stodieck, D. M. Klaus, W. W. Adams III and W. J. Emery, *Int. J. Remote Sens.*, 2008, **29**, 3701–3713.
64 M. Yu, J. Li, W. Sun, M. Jiang and F. Zhang, *J. Mater. Sci.*, 2014, **49**, 5519–5528.
65 S. Cherian and C. C. Wamser, *J. Phys. Chem. B*, 2000, **104**, 3624–3629.
66 A. T. Gallagher, J. Y. Lee, V. Kathiresan, J. S. Anderson, B. M. Hoffman and T. D. Harris, *Chem. Sci.*, 2018, **9**, 1596–1603.

67 M. D. Aljabri, D. D. La, R. W. Jadhav, L. A. Jones, D. D. Nguyen, S. W. Chang, L. D. Tran and S. V. Bhosale, *Fuel*, 2019, **254**, 115639.
68 M. Massaro, S. Riela, P. Lo Meo, R. Noto, G. Cavallaro, S. Milioto and G. Lazzara, *J. Mater. Chem. B*, 2014, **2**, 7732–7738.
69 The density of the perfluorinated porphyrin was obtained by the Royal society of chemistry website **https://chemspider.com/Chemical-Structure.26563579.html**.
70 W. Wei, R. Minullina, E. Abdullayev, R. Fakhrullin, D. Mills and Y. Lvov, *RSC Adv.*, 2014, **4**, 488–494.
71 M. Notarbartolo, M. Massaro, R. de Melo Barbosa, C. Emili, L. F. Liotta, P. Poma, F. M. Raymo, R. Sànchez-Espejo, R. Vago, C. Viseras-Iborra and S. Riela, *Colloids Surf., B*, 2022, **220**, 112931.
72 C. Zhang, K. Yan, C. Fu, H. Peng, C. J. Hawker and A. K. Whittaker, *Chem. Rev.*, 2022, **122**, 167–208.